Acta Pharmaceutica Sinica B 2026;16(7):4350−4366

Chinese Pharmaceutical Association
Institute of Materia Medica, Chinese Academy of Medical Sciences

Acta Pharmaceutica Sinica B

www.elsevier.com/locate/apsb
www.sciencedirect.com

ORIGINAL ARTICLE

Hepatic stellate cell enriched Asporin drives liver fibrosis by stabilizing ERH to promote IL-17/MAPK11 signaling

Jian Sun[a,b,†], Ruoxuan Yang[a,†], Mengmeng Liu[a,†], Yi Chen[a,†], Yu Zhang[a], Huiying Gao[a], Zhiwei Ning[a], Shifen Li[a], Dina Saifullina[a], Xiaomu Tian[a], Tongzhu Jin[a], Yingying Guo[a], Qianqian Wang[a], Yixin Zhang[a], Tengfei Pan[a], Yu Bian[a], Erliang Guo[c], Yanyan Liu[d,*], Jing Liu[e,*], Tianyu Li[a,f,*], Haihai Liang[a,*]

[a]*State Key Laboratory of Frigid Zone Cardiovascular Diseases (SKLFZCD), Department of Pharmacology (State Key Laboratory-Province Key Laboratories of Biomedicine-Pharmaceutics of China, Key Laboratory of Cardiovascular Research, Ministry of Education), College of Pharmacy, Harbin Medical University, Harbin 150081, China*
[b]*Translational Medicine Research Center, Medical Pathology Center, Chongqing University Three Gorges Hospital, School of Medicine Chongqing University, Chongqing University, Chongqing 404000, China*
[c]*Department of Thoracic Surgery, Harbin Medical University Cancer Hospital, Harbin 150081, China*
[d]*Zhuhai People's Hospital (The Affiliated Hospital of Beijing Institute of Technology, Zhuhai Clinical Medical College of Jinan University), Zhuhai 519000, China*
[e]*Digestive Department, Second Affiliated Hospital of Harbin Medical University, Harbin 150086, China*
[f]*Department of Physiology, School of Basic Medical Sciences, Harbin Medical University, Harbin 150081, China*

Received 11 September 2025; received in revised form 10 December 2025; accepted 4 January 2026

KEY WORDS

Liver fibrosis;
Hepatic stellate cells;
Asporin;
Non-invasive biomarker;

Abstract Liver fibrosis is a pathological process primarily driven by activated hepatic stellate cell (HSC). Single-cell transcriptomics of human fibrotic livers identified *ASPN* (Asporin) as highly expressed in inflammatory and fibrogenic HSC subsets. Clinically, Asporin was markedly elevated in liver tissue and serum, correlating with fibrosis stage across datasets and cohorts, supporting its potential as a non-invasive biomarker. Functionally, Asporin promoted HSC activation and extracellular matrix

*Corresponding authors.
E-mail addresses: lianghaihai@ems.hrbmu.edu.cn (Haihai Liang), hrbmulty@126.com (Tianyu Li), 0liujing@163.com (Jing Liu), liuyanyan_90@ext.jnu.edu.cn (Yanyan Liu).
[†]These authors made equal contributions to this work.
Peer review under the responsibility of Chinese Pharmaceutical Association and Institute of Materia Medica, Chinese Academy of Medical Sciences.

https://doi.org/10.1016/j.apsb.2026.03.045

ERH;
Extracellular matrix remodeling;
MAPK11;
Prasugrel

(ECM) remodeling, whereas its depletion reduced fibrosis in CCl_4-induced mouse models. Mechanistically, Asporin bound directly to ERH and stabilized it by preventing ubiquitin-mediated degradation. Structural modeling showed Asporin masked ERH's K12 ubiquitination site *via* hydrogen bonds and hydrophobic interactions. ERH overexpression in HSC activated fibrogenic genes and IL-17 signaling, converging on MAPK11 as a common downstream effector. Notably, ERH knockdown abrogated Asporin-driven profibrotic responses. High throughput screening identified prasugrel, a clinically approved drug, as a potent Asporin suppressor. In CCl_4 and high-fat diet induced fibrosis models, prasugrel alleviated fibrosis, inflammation, lipid accumulation, and portal hypertension by suppressing Asporin and ERH expression. Collectively, these findings define the Asporin/ERH/IL-17/MAPK11 axis as a key mediator of HSC activation and fibrogenesis and highlight prasugrel as a promising anti-fibrotic therapy.

1. Introduction

Liver fibrosis is a progressive pathological condition characterized by excessive extracellular matrix (ECM) deposition in response to chronic liver injury. It represents a common final pathway of diverse liver diseases, including viral hepatitis, alcohol-related liver disease, and metabolic-associated steatotic liver disease (MASLD)[1,2]. If left unresolved, persistent fibrosis can lead to cirrhosis, liver failure, and hepatocellular carcinoma, placing a substantial global health burden on society[3,4].

Effective management of liver fibrosis relies heavily on early detection and timely intervention. Current non-invasive diagnostic tools for fibrosis staging, such as serum biomarkers and imaging-based indices (FIB-4, elastography)[5,6], lack specificity and are insufficiently predictive of disease progression or treatment response. Although the enhanced liver fibrosis (ELF) test shows overall good diagnostic performance for staging hepatic fibrosis, its accuracy varies substantially across different disease etiologies and fibrosis stages[7]. This diagnostic gap underscores the need for more mechanistically relevant, non-invasive biomarkers capable of identifying fibrosis progression at an earlier stage.

Despite advances in understanding liver disease pathogenesis[8-10], no approved anti-fibrotic therapy has effectively reversed established fibrosis, largely due to incomplete knowledge of the molecular mechanisms driving hepatic stellate cell (HSC) activation and maintaining the fibrogenic niche[11,12]. HSC, the principal source of fibrillar collagen in fibrotic liver, undergoes a transition to a myofibroblastic state upon injury, governed by complex signaling and transcriptional reprogramming[13]. However, key regulators of this process remain poorly defined, limiting biomarker discovery and therapeutic development. Single-cell transcriptomics has revealed HSC heterogeneity and novel activated subsets[14,15], but few studies have linked these subsets to actionable molecular targets.

Motivated by these gaps, we sought to identify novel molecular drivers of HSC activation and liver fibrosis progression through multi-dimensional approach. Leveraging single-cell RNA sequencing of fibrotic and non-fibrotic liver tissues, we identified *ASPN*, coding for Asporin, a small leucine-rich proteoglycan, as a candidate gene highly enriched in activated HSC subpopulations.

Originally described for its role in cartilage matrix organization, Asporin has since been implicated in multiple fibrotic and tumor-associated contexts. In systemic sclerosis, *ASPN* positive fibroblasts synergize with endothelial cells to promote skin fibrosis, supporting its fibrogenic potential[16]. Asporin has been identified as a mesenchymal-derived ECM component that regulates stromal niche remodeling and tissue repair, as demonstrated in intestinal regeneration models[17]. Moreover, Asporin has been directly implicated in fibrotic remodeling, where suppression of Asporin in cardiac fibroblasts reduced myocardial fibrosis and calcification, highlighting its functional role in fibroblast-mediated matrix deposition[18]. Furthermore, Asporin has also been identified as a pro-tumorigenic factor, where it facilitates prostate cancer chemoresistance and metastatic progression through activation of Wnt/β-catenin signaling[19]. Kumagai et al.[20] demonstrated that serum Asporin levels significantly fluctuated before and after laparoscopic sleeve gastrectomy in non-alcoholic fatty liver disease (NAFLD) patients, suggesting its potential as a biomarker. Despite these emerging roles, the function of Asporin in liver fibrosis has remained largely unexplored.

In light of the current deficiency in reliable diagnostic markers and effective therapeutic targets for liver fibrosis, we identified *ASPN* as a stromal gene enriched in activated hepatic stellate cells *via* single-cell transcriptomics. We validated its diagnostic potential in tissue and serum, and demonstrated that Asporin promotes HSC activation by stabilizing the nuclear factor ERH and enhancing fibrogenic gene expression. High throughput screening further identified prasugrel as an Asporin inhibitor that alleviates fibrosis in mouse models. These findings position Asporin as a promising candidate for the diagnosis and treatment of liver fibrosis.

2. Materials and methods

2.1. Human samples

Patient samples were collected from the Second Affiliated Hospital of Harbin Medical University, with all procedures approved by the hospital's Institutional Review Board (Ethics approval number: KY2024-159). Informed consent was attained from all patients. Liver tissues were obtained from patients undergoing liver surgery. The severity of fibrosis was evaluated based on hematoxylin and eosin (H&E) staining. Patient characteristics are listed in Supporting Information Table S1.

Peripheral blood samples were collected from patients with liver fibrosis of various etiologies, including alcoholic cirrhosis, autoimmune liver disease, NAFLD, hepatitis B, hepatitis C and non-alcoholic steatohepatitis. Detailed clinical information for these patients is provided in Supporting Information Table S2.

2.2. Animals and treatment

All experiments complied with the guiding principles for the care and use of laboratory animals and were approved by the Ethics Committee for Animal Experimentation of the College of Pharmacy, Harbin Medical University (Approval No. 5038724).

Male C57BL/6 mice (8−10 weeks) were purchased from Changsheng Biotechnology (Liaoning, China) and housed in a specific pathogen-free facility under a 12 h light/12 h dark cycle at 23 ± 3 °C and 30%−70% relative humidity. Mice were given *ad libitum* access to food and water and were randomly assigned to experimental groups.

Aspn global knockout mice (*Aspn*-KO), *Aspn* flox/flox mice, and Lrat-Cre transgenic mice were custom generated on a C57BL/6 background by Cyagen Biosciences Inc. (Suzhou, China). *Aspn* flox/flox mice were crossed with Lrat-Cre mice to generate hepatic stellate cell specific *Aspn* conditional knockout mice ($Aspn^{HSC-KO}$), and genotyping was performed *via* PCR using tail DNA.

Three murine models of liver fibrosis were established. In the CCl_4-induced fibrosis model, mice received intraperitoneal injections of 10% CCl_4 (HY-Y0298, MedChemExpress LLC, Shanghai, China; 2 mL/kg body weight, diluted in olive oil) twice weekly for 6 weeks. In the hybrid fibrosis model, mice were fed a high-fat diet (HFD, D12492, Xiao Shu You Tai Biotechnology Co., Ltd., Beijing, China) from Day 1 to Day 28 and were intraperitoneally injected with CCl_4 on Days 16, 19, 23, and 26 to mimic metabolic and toxicant associated liver injury. Bile duct ligation was performed under anesthesia by double ligating and transecting the common bile duct using sterile surgical procedures. Sham-operated mice underwent laparotomy and bile duct exposure without ligation. Liver tissues and serum were collected 18 days after surgery for biochemical, histological, and molecular analyses.

Prasugrel (HY-10112, MedChemExpress, China) was administered by oral gavage at 2 mg/kg every other day. In the preventive treatment group, prasugrel was administered from Day 1 to Day 42. In the therapeutic treatment group, prasugrel was administered from Day 28 to Day 42 after establishment of liver fibrosis.

2.3. Cell lines

LX2 (human HSC line) and HSC-T6 (rat HSC line) were purchased from Shanghai Xinyu Biotechnology Co., Ltd. LX2 were cultured in a standard medium comprising RPMI 1640 (C11875500BT; Gibco), 10% FBS (BC-SE-FBS07; Bio-channel), and 1% penicillin−streptomycin (P7630; Solarbio). LX2 were placed in 5% CO_2 under a water-saturated atmosphere in a cell incubator at 37 °C. AML-12 cells were kindly provided by Professor Yang Zhang from Harbin Medical University and cultured in DMEM/F12 medium supplemented with 10% fetal bovine serum (FBS), 0.5% ITS-G (100 ×), 40 ng/mL dexamethasone, and 1% penicillin−streptomycin.

2.4. Cell transfection and treatment

For plasmid or siRNA transfection, cells were transfected with either 20 nmol/L siRNA or plasmid at a final concentration of 2 μg/mL using Lipofectamine™ 2000 (Invitrogen, USA), following the manufacturer's instructions.

Adenovirus vector encoding *ASPN* was generated by Hanheng Biotechnology (Shanghai, China). For adenoviral infection LX2 cells (8×10^4 cells/well) were seeded in well plates one day before transduction. When cells reached 30%−50% confluence, they were infected with adenovirus carrying either vector control or Adv-*ASPN* in half-volume medium at a multiplicity of infection of 300. The infection was performed at 37 °C for 4 h, after which the medium was replaced with fresh complete culture medium. Cells were collected 48 h later for further analysis.

2.5. Single-cell RNA sequencing and preprocessing

The publicly available scRNA-seq data (GEO accession numbers GSE136103 and GSE186343) for liver tissue samples from patients diagnosed with fibrosis ($n = 15$) and healthy controls ($n = 11$) were used for analyses. The Scanpy package was used for analysis by importing the raw count matrices. Low-quality cells were excluded as determined by the number of genes (less than 300 or more than 3000), UMI counts (more than 30,000) and the percentage of mitochondrial reads (more than 25%).

UMI counts were normalized and log-transformed. The top 3000 highly variable features were identified and scaled using the highly_variable_genes and scale functions. Principal component analysis and nonlinear dimensional reduction UMAP were applied to perform dimensional reduction. The harmony method was used for batch correction. The neighborhood graph of cells using the adjusted PCA representation were clustered using leiden cluster methods. Cluster annotation was based on established marker genes. Trajectory inference and pseudotime analyses were conducted using Monocle3. The differentially expressed genes between $ASPN^+$Stellate cells and $ASPN^-$ Stellate cells were identified using the Wilcoxon rank-sum test.

2.6. Biomarker validation and statistical analysis

The publicly available bulk RNA-seq data (GEO accession numbers GSE240729, GSE174478, GSE84044, GSE152329 and GSE246221) for fibrotic liver tissue samples were used for analyses. Correlation analyses between *ASPN* expression and fibrosis or inflammation stages were performed using Pearson correlation tests. ROC curves were generated to evaluate the predictive performance of *ASPN* expression for FIB-4 and FIB-5 indices.

2.7. Sample bias of stellate cell subtypes

We calculated the ratio of observed to expected cell numbers $\log_2(R_{e/o})$ for each cluster in different tissues to quantify the tissue preference of each cluster. The expected cell numbers for each combination of cell clusters and sample types were obtained from the chi-square test. Cell type was identified as normal-enriched if $R_{e/o} > 0$, else fibrosis-enriched.

2.8. Quantitative real-time PCR (qRT-PCR)

Total RNA was extracted from cells or tissues using TRIzol reagent (Invitrogen, Carlsbad, USA) according to the manufacturer's instructions. Reverse transcription was performed using a qPCR RT Kit (TOYOBO Co., Ltd., Osaka, Japan) following the manufacturer's protocol. The reaction conditions were as follows: 37 °C for 15 min, 98 °C for 5 min, and hold at 4 °C. cDNA synthesis was carried out in a total reaction volume of 10 μL. Quantitative PCR was performed using SYBR Green Master Mix (Roche, Basel, Switzerland) on a StepOne Real-Time PCR System (Applied Biosystems). Relative gene expression was calculated using the

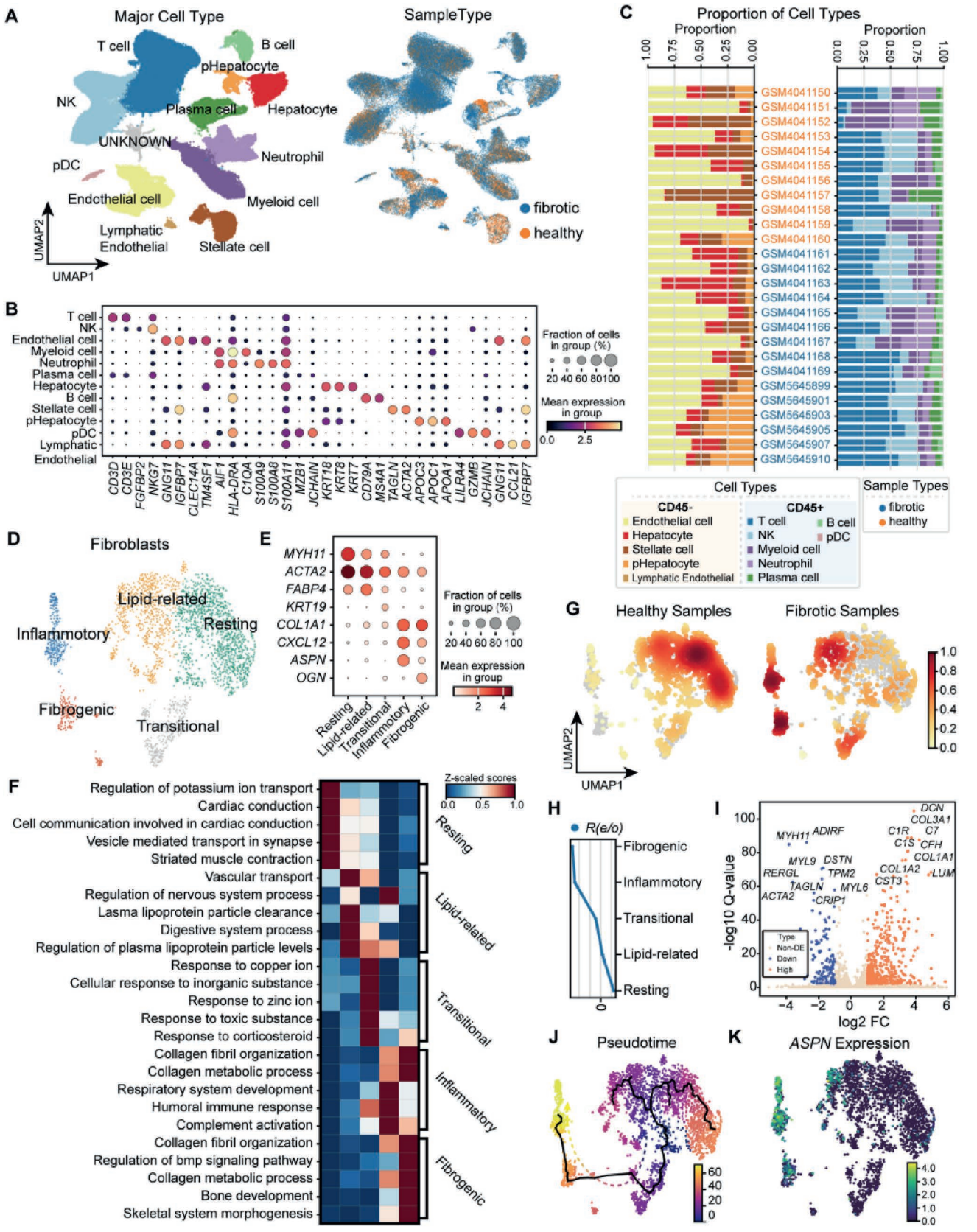

Figure 1 Single-cell characterization of liver fibrosis and *ASPN* expression analysis. (A) UMAP visualization of major liver cell types from fibrotic and healthy liver samples. Different colors represent cell types and sample types, respectively. (B) Dot plot showing the classic markers for each cell type. (C) Bar plot showing the proportion of each cell type across fibrotic and healthy liver samples. Left, proportion of various cell types in $CD45^-$ stromal or epithelial cells. Right, proportion of various cell types in $CD45^+$ immune cells. (D) UMAP plot displaying sub-clusters of

$2^{-\Delta\Delta CT}$ method. All primers are listed in Supporting Information Table S3.

2.9. Western blot

Proteins were extracted from cultured cells or liver tissues and separated by SDS-PAGE. The proteins were then transferred onto PVDF membranes, followed by blocking with 5% non-fat milk in TBST at room temperature for 1 h. Membranes were incubated overnight at 4 °C with primary antibodies. GAPDH (Affinity, 60004-1-1g) was used as a loading control. The following primary antibodies were used: ERH (Proteintech, 15974-1-AP), FN1 (Bioworld, BS41340), Collagen I (Wanleibio, WL0088), α-SMA (Abconal Inc., BF9212), Asporin (Affinity, DF13642), and Desmin (Proteintech, 16520-1-AP). After washing, membranes were incubated with appropriate secondary antibodies. Protein bands were visualized and quantified using Odyssey Image Studio software (version 5.2).

2.10. GST (glutathione S-transferase) pull-down assays

GST or GST-ASPN fusion proteins were expressed in *E. coli* and purified using Glutathione Sepharose 4B resin pre-equilibrated in binding buffer (PBS containing 0.1% Triton X-100). Equal amounts of immobilized GST or GST-ASPN were incubated with clarified cell lysates at 4 °C for 3 h with rotation. Beads were washed 5 times with binding buffer, and bound proteins were eluted with 15 mmol/L reduced glutathione. Eluates were resolved by SDS-PAGE and analyzed by Coomassie/silver staining for MS identification or by immunoblotting with antibodies against candidate interactors.

2.11. Ubiquitination site prediction

The full-length amino acid sequence of human ERH (UniProt ID: Q9H4Z2) was retrieved from the UniProt database. All lysine (K) residues were identified, and a sequence-based prediction was performed using an approach modeled after UbPred[21]. Each lysine residue was evaluated within a ±6 amino acid sliding window, considering sequence context features such as amino acid composition, disorder propensity, and hydrophobicity. A custom scoring system was applied, with prediction values ranging from 0 to 1. In addition, the potential ubiquitination sites of ERH were queried using the PhosphoSitePlus® database.

2.12. Protein binding region prediction

The protein sequences of Asporin and ERH were obtained from the UniProt database and subsequently utilized as input for a single run of the AlphaFold2 algorithm. This process generated five models per run, employing the AlphaFold2 Multimer v2.3 model parameters. AlphaFold2 evaluates model quality using four metrics: predicted Local Distance Difference Test (pLDDT), predicted Template Modeling score (pTMscore), inter-chain predicted Template Modeling score (ipTMscore), and model confidence score. The protein structure model exhibiting the highest confidence, as determined by the confidence ranking, was selected for further analysis. The predicted binding site of the Asporin-ERH complex was subjected to visual analysis utilizing PyMOL (version 3.0.3). The protein structures of Asporin and ERH were loaded and assigned distinct colors. Subsequently, PyMOL's "find-polar contacts" function was used to identify hydrogen bonds between Asporin and ERH.

2.13. Immunofluorescence staining

LX2 cells were cultured in 24 well plates and were treated when the cell density reached 60%. They were washed 3 times in PBS, fixed with 500 μL of 4% paraformaldehyde at 37 °C for 15 min, incubated with 500 μL of penetration solution for 1 h at room temperature, blocked with 1 mL of 5% goat serum (goat serum: PBS = 1:1) for 1 h. Primary antibody was incubated at 4 °C overnight. The next day it was incubated with the secondary antibody for 1 h; the DAPI was stained for 7 min at room temperature. Cell fluorescence intensity was observed under a fluorescence microscope.

Liver lobes were embedded in OCT (Sakura, Finetek, Japan) and sliced into 5 μm thick sections. The frozen sections were fixed with acetone, after which peroxidase activity was blocked by treatment with 3% H_2O_2, and the tissue sections were then incubated with primary antibodies specific for α-SMA (Affinity Inc., BF9212), Collagen I (Proteintech, 66900-1-Ig), Asporin (Affinity, DF13642), Desmin (Proteintech, 16520-1-AP) and ERH (Santa, sc-373906). DAPI was used to label nuclei. Images were acquired using a confocal microscope (FluoView FV10i, Olympus, Tokyo, Japan).

2.14. Proliferation assays

Cell Light EdU Apollo 567 *In Vitro* Kit (RiboBio, Guangzhou, China) was used to detect cell proliferation. LX2 cells were cultured in 24-well plates. After transfection for 48 h, EdU incorporation was performed according to the manufacturer's protocol. EdU-positive cells were imaged by fluorescence microscopy and quantified.

2.15. Wound-healing assay

The cells were cultured in 6-well plates overnight to determine the migration ability of hepatic stellate cells. The cell monolayer was scratched on the tip of 200 μL plastic micropipette and cultured under standard culture conditions. Then the cells were observed with Nikon Ts100 microscope (Nikon, Tokyo, Japan) at 0 and 24 h.

2.16. Cell contraction assay

Cells were harvested and resuspended in desired medium at $2 \times 10^6 - 5 \times 10^6$ cells/mL. Prepare the cell contraction matrix by mixing 2 parts of cell suspension and 8 parts of cold Collagen Gel

stellate cells identified as Resting, Lipid-related, Transitional, Fibrogenic, and Inflammatory. (E) Density plot indicating the cell density in healthy and fibrotic samples. (F) Functional enrichment heatmap showing GO terms significantly enriched in stellate subtype cells. (G) Dot plot indicating the marker gene expression of stellate cell subsets, with *ASPN* highly expressed in inflammatory stellate cells. (H) The $\log_2(R_{e/o})$ of cell numbers illustrates the sample bias of stellate cell subtypes. (I) Volcano plot showing differentially expressed genes between *ASPN* positive ($ASPN^+$) and ASPN negative ($ASPN^-$) stellate cells. (J) Pseudotime trajectory plot illustrating the transition from Resting to Inflammatory stellate cells. (K) UMAP plot of *ASPN* gene expression across the pseudotime trajectory. $R_{e/o}$, Expected-over-Observed ratio.

Working Solution. Add 0.5 mL of the cell contraction matrix to each well of the 24 well Cell Contraction Plate. Incubate the plate at 37 °C and 5% CO_2 for 1 h. After collagen polymerization, carefully add 1.0 mL of culture medium (with/without contraction mediators) atop each collagen gel lattice. Monitor wells for contraction over 2 days at 37 °C and 5% CO_2. Media should be changed daily by carefully removing 0.5 mL and replacing with 0.5 mL fresh media (with/without contraction mediators). The collagen gel images were taken at 0, 12, and 24 h.

2.17. Ultrasound imaging measurement

Liver echography was performed to non-invasively assess hepatic steatosis and fibrosis. Mice were anesthetized by intraperitoneal injection of Avertin (250 mg/kg), and ultrasound coupling gel was applied to the upper abdominal region. A 30-MHz transducer (Vevo® 2000 system) was positioned over the left upper abdomen to visualize the liver and portal vein. B-mode images were acquired in a modified short-axis view to capture the hepatic parenchyma. The portal vein was further imaged in a long-axis view, and both B-mode and M-mode images were collected for hemodynamic assessment.

2.18. Histological analysis

Paraffin-embedded liver sections (5 μm) were dewaxed in xylene, rehydrated through graded ethanol, and incubated with 3% hydrogen peroxide for 10 min to block endogenous peroxidase activity. Antigen retrieval was performed as needed, followed by blocking in goat serum. Sections were incubated overnight at 4 °C with primary antibodies, then with HRP-conjugated secondary antibodies for 30 min at room temperature. Signals were developed using DAB substrate, counterstained with hematoxylin, dehydrated, and mounted with neutral resin.

For Masson's trichrome staining (Solarbio, Beijing, China), dewaxed sections were sequentially stained with hematoxylin, ponceau acid fuchsin, and aniline blue according to the manufacturer's instructions.

H&E staining was performed to assess general histopathology. Dewaxed sections were stained with hematoxylin for 5 min, differentiated in acid alcohol, rinsed in water, and stained with eosin for 30 s. Slides were dehydrated, cleared, and mounted.

Oil Red O staining was performed on 8 μm frozen liver sections embedded in OCT. Sections were fixed in 4% paraformaldehyde, stained with Oil Red O solution, and counterstained with hematoxylin to visualize lipid droplets.

All stained sections were imaged using a bright field microscope (LEICA, Germany), and quantitative analyses were performed using ImageJ software.

2.19. Biochemical assays of liver function and hydroxyproline content

Liver function markers, including total cholesterol (TC), aspartate aminotransferase (AST/GOT), and alanine aminotransferase (ALT/GPT), were quantified using commercial kits according to the manufacturer's instructions. Specifically, TC levels were assessed using the Total Cholesterol Assay Kit (Elabscience, E-BC-K109-M), AST activity using the AST Activity Assay Kit (Elabscience, E-BC-K236-S), and ALT activity using the ALT Activity Fluorometric Assay Kit (Elabscience, E-BC-F038).

To evaluate collagen deposition, hepatic hydroxyproline content was measured using a Hydroxyproline Assay Kit (Nanjing Jiancheng Bioengineering Institute, China) following the manufacturer's protocol.

2.20. Cell-based high-throughput screening for Asporin inhibitors

An EGFP-tagged human *ASPN* expression plasmid (CMV promoter-driven, C-terminal fusion) was stably transfected into HEK293 cells using Lipofectamine 2000. For screening, EGFP-*ASPN*-HEK293 cells were seeded in 384-well plates and treated with a library of 3105 FDA-approved compounds (10 μmol/L final concentration, Cat. No. L1300, Selleck, Shanghai, China) for 48 h. Fluorescence intensity was quantified using a plate reader (ex/em: 488 nm/509 nm). Top candidate compounds were subsequently subjected to secondary functional validation in LX2 hepatic stellate cells to confirm suppression of ASPN expression and fibrogenic responses by qRT-PCR.

2.21. Co-immunoprecipitation

FLAG-*ASPN* was expressed in cells *via* plasmid transfection. Cell lysates were prepared using IP lysis buffer (Abbkine, BMP2020) and subjected to immunoprecipitation with an anti-FLAG antibody (66008-4-Ig, Proteintech) and Protein A/G Magnetic Beads (MedChemExpress, HY-K0202). The precipitated complexes were washed extensively and then analyzed by Western blotting to detect co-precipitated endogenous ERH protein.

2.22. Surface plasmon resonance (SPR) analysis

SPR experiments were performed on a Biacore 1K system using CM5 chips and standard amine-coupling chemistry. ERH and Asporin proteins were immobilized on flow cells 2 and 4 in 10 mmol/L sodium acetate buffer (pH 4.5), with reference channels prepared in parallel. Binding measurements were conducted in PBS-P+ buffer (pH 7.4, 5% DMSO) at 30 μL/min. Prasugrel or recombinant Asporin was injected in a concentration series for 60 s, followed by regeneration with 10 mmol/L glycine-HCl (pH 2.0). Sensorgrams were double referenced and globally fitted to a 1:1 Langmuir model to derive kinetic parameters.

2.23. Statistical analysis

Data are expressed as the mean ± standard error of mean (SEM) of at least three independent experiments for each experimental group. Student's *t* test was used for comparisons between two groups, one-way analysis of variance followed by Tukey corrected *post hoc t* test was used for multi-group comparisons. $P < 0.05$ was considered statistically significant.

3. Results

3.1. Single-cell profiling of liver samples identifies cell types enriched in fibrosis

We conducted an analysis of RNA-sequencing data sourced from two publicly accessible databases, encompassing samples from both healthy individuals and patients diagnosed with liver fibrosis (Fig. 1A). Unsupervised clustering identified major hepatic cell

types, including immune cells, endothelial cells, hepatocytes, and stellate cells (Fig. 1B). The relative proportion showed an increased fraction of stellate cells in fibrotic liver samples compared to healthy controls, indicating a potential role in fibrosis pathogenesis (Fig. 1C). Global analysis across hepatic cell types showed that *ASPN* expression was highly restricted to stellate cells, and its expression levels were substantially elevated in stellate cells from fibrotic liver samples relative to healthy controls (Supporting Information Fig. S1A and S1B).

Given the central role of stellate cells in liver fibrosis, we performed high-resolution sub-clustering and identified five distinct HSC states, including resting, lipid-related, transitional, inflammatory, and fibrogenic subtypes (Fig. 1D). Differential gene expression analysis revealed that *ASPN* is highly and specifically expressed in the inflammatory and fibrogenic stellate cells (Fig. 1E), which represented the major activated HSC populations in fibrotic livers and showed the strongest enrichment of fibrosis-related pathways, including collagen fibril organization, ECM remodeling, and cytokine signaling (Fig. 1F). Both activated subtypes (inflammatory and fibrogenic stellate cells) were enriched in fibrotic liver samples (Fig. 1G and H). Comparison of *ASPN*$^{+}$*versus ASPN*$^{-}$ stellate cells demonstrated that *ASPN*$^{+}$cells expressed significantly higher levels of collagen genes, including *COL1A1* and *COL3A1*, highlighting *ASPN* as a marker of highly fibrogenic HSC (Fig. 1I). Pseudotime trajectory analysis further showed a progressive increase in *ASPN* expression along the activation path from resting to inflammatory/fibrogenic HSC (Fig. 1J and K), supporting its association with HSC activation

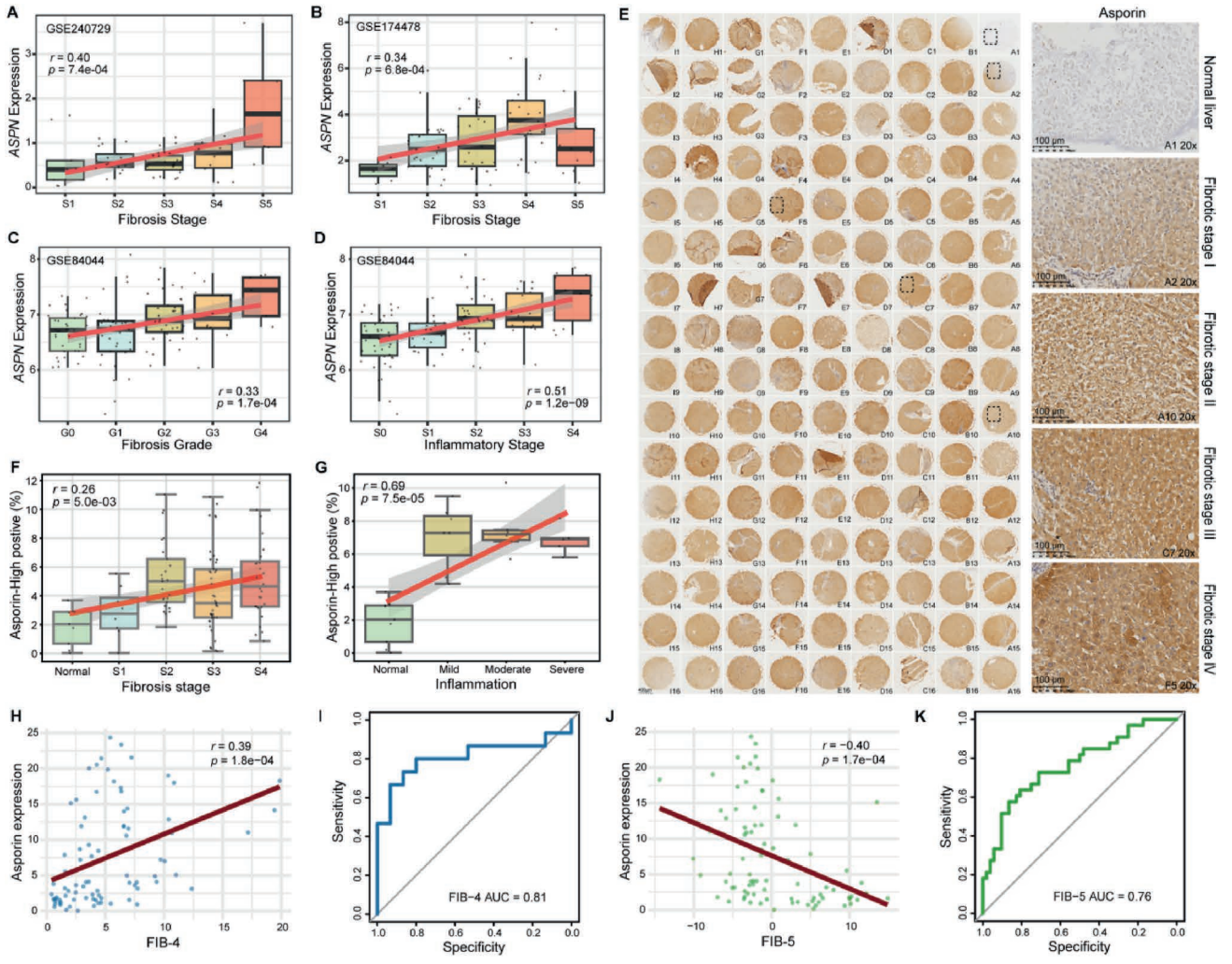

Figure 2 Asporin is associated with liver fibrosis progression and shows potential as a diagnostic biomarker. (A) Correlation between *ASPN* mRNA expression and fibrosis stage in liver tissue from 67 patients with metabolic dysfunction-associated steatotic liver disease (GSE240729). (B) Positive correlation between *ASPN* expression and fibrosis stage in 94 patients with non-alcoholic fatty liver disease (GSE174478). (C, D) In 124 patients with chronic hepatitis B, *ASPN* expression correlated with both fibrosis stage and inflammation grade (GSE84044). (E) Representative immunohistochemical staining of Asporin in liver tissues with increasing fibrosis severity. (F, G) Quantification of Asporin staining using ImageJ showed positive correlations with fibrosis stage ($n = 87$) and inflammation grade ($n = 32$). (H−K) Serum Asporin protein levels in 99 patients (including viral hepatitis, NAFLD, alcoholic hepatitis, autoimmune hepatitis, and primary biliary cholangitis) with liver fibrosis or cirrhosis were measured by ELISA. (H) Serum Asporin levels positively correlated with FIB-4, (I) AUC = 0.81. (J) Serum Asporin levels negatively correlated with FIB-5, (K) AUC = 0.76.

dynamics. Cross-cell communication analysis revealed that inflammatory HSC actively interacted with NK cells, neutrophils, T cells, and pDCs through ligand receptor pairs such as ICAM1−ITGAL and CD40−CD74, suggesting their role in shaping a pro-fibrotic immune microenvironment (Supporting Information Fig. S2A−S2C). Together, these results identify *ASPN* as a selectively enriched, activation associated molecule in pathogenic HSC subpopulations.

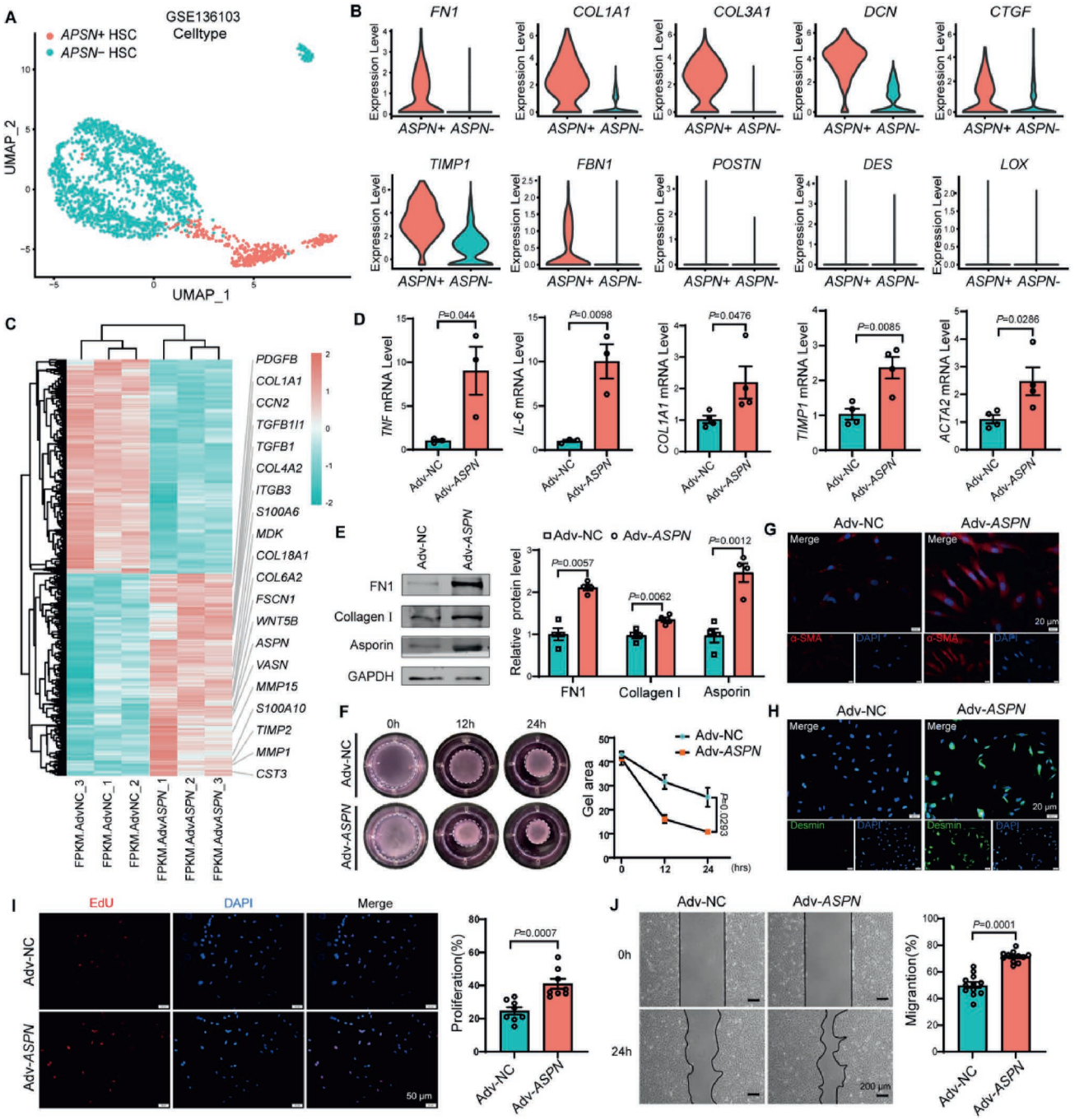

Figure 3 Asporin promotes activation of hepatic stellate cells. (A) HSCs from cirrhotic liver single-cell RNA-seq data (GSE136103) were divided into $ASPN^{+}$ and $ASPN^{-}$ subpopulations for differential expression analysis. (B) Violin plot showing elevated expression of fibrosis related genes (*FN1*, *COL1A1*, *COL3A1*, *DCN*, *CTGF*, *TIMP1*, *FBN1*, *POSTN*, *DES*, *LOX*) in $ASPN^{+}$HSCs. (C) RNA-seq was performed on LX2 cells following *ASPN* overexpression to assess its functional impact. Differential expression analysis identified 1566 upregulated and 1664 downregulated genes ($q < 0.05$). (D) qRT-PCR analysis showing that *ASPN* overexpression in LX2 cells upregulates *IL6, TNF* mRNA ($n = 3$) and *COL1A1*, *TIMP1*, *ACTA2* mRNA expression ($n = 4$). (E) Western blot analysis confirming increased FN1 and collagen I protein levels upon *ASPN* overexpression ($n = 4$). (F) Collagen gel contraction assay showing enhanced ECM remodeling in *ASPN* overexpressing cells ($n = 3$). (G, H) Immunofluorescence staining showing increased α-SMA and Desmin expression in *ASPN* overexpressing LX2 cells ($n = 3$, bar = 20 μm). (I, J) EdU proliferation assay ($n = 4$, two images were taken for each group, bar = 200 μm) and Wound healing assay ($n = 6$, two images were taken for each group, bar = 50 μm) demonstrating enhanced proliferation and migration in *ASPN*-overexpressing LX2 cells.

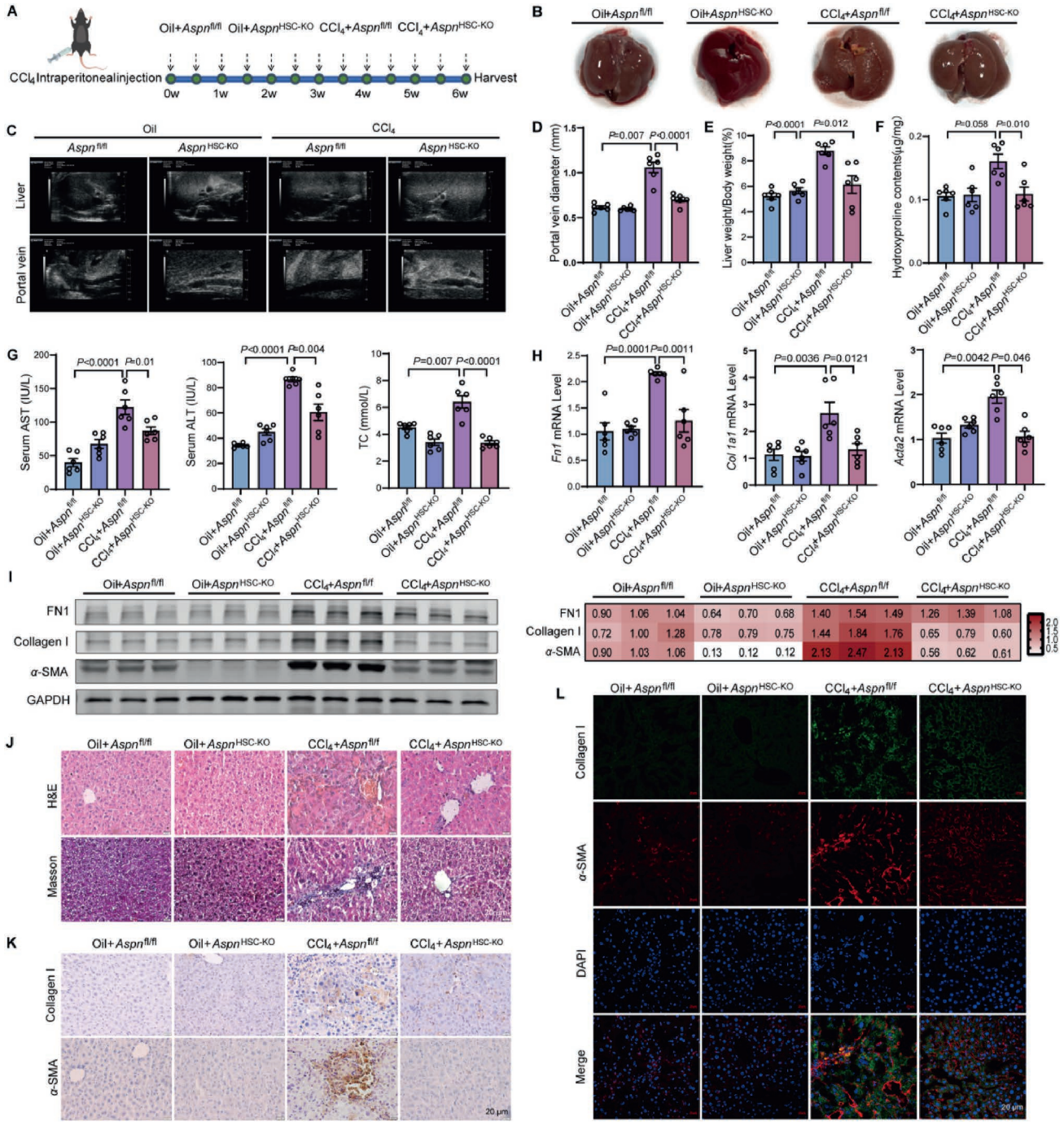

Figure 4 Hepatic stellate cell-specific deletion of *Aspn* alleviates liver fibrosis in mice. (A) Schematic of the experimental workflow. Liver fibrosis was induced in *Aspn*-flox and HSC-specific *Aspn* conditional knockout ($Aspn^{HSC\text{-}cKO}$) mice *via* intraperitoneal injection of CCl_4. (B) Representative gross liver morphology ($n = 6$). (C) Representative ultrasound images of liver and portal vein ($n = 6$). (D) Quantification of Doppler ultrasound measurements of portal vein diameter ($n = 6$). (E, F) Liver-to-body weight ratio and hepatic hydroxyproline content were significantly reduced in $Aspn^{HSC\text{-}cKO}$ mice compared to flox controls ($n = 6$). (G) Serum ALT, AST, TC levels were elevated in the CCl_4+$Aspn^{fl/fl}$ group and reduced in $Aspn^{HSC\text{-}cKO}$ mice ($n = 6$). (H) qRT-PCR analysis showing decreased *Fn1*, *Col1a1* and *Acta2* mRNA expression in $Aspn^{HSC\text{-}cKO}$ livers ($n = 6$). (I) Western blot analysis confirming lower protein levels of FN1, collagen I, and α-SMA in $Aspn^{HSC\text{-}cKO}$ mice ($n = 3$). (J) Representative H&E and Masson's trichrome staining showing reduced inflammation and collagen deposition in $Aspn^{HSC\text{-}cKO}$ livers ($n = 3$, bar = 50 μm). (K, L) Immunohistochemistry and immunofluorescence staining showing decreased expression of Collagen I and α-SMA in $Aspn^{HSC\text{-}cKO}$ livers ($n = 3$, bar = 20 μm).

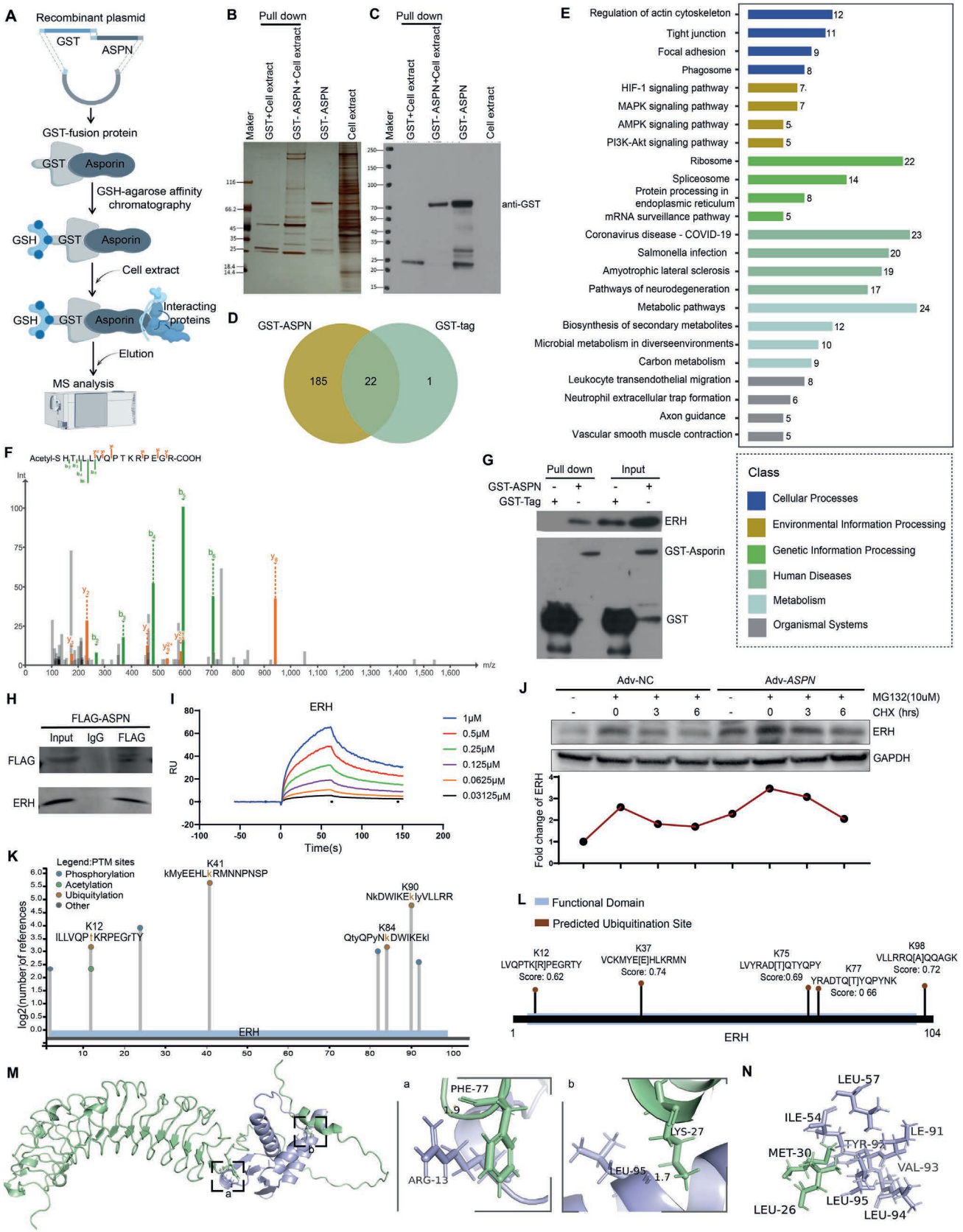

Figure 5 Asporin interacts with and stabilizes ERH *via* inhibition of ubiquitination and proteasomal degradation. (A) Schematic overview of GST pull-down. (B, C) Silver staining and Western blot confirming successful construction and purification of GST-ASPN fusion protein. (D) Venn diagram showing 185 Asporin-specific interacting proteins identified by mass spectrometry. (E) KEGG enrichment analysis of Asporin-binding proteins. (F) Representative MS/MS fragmentation spectrum showing ERH was Asporin-binding partner. (G) GST pull-down

3.2. Asporin expression is enriched in fibrogenic stellate cells and correlates with fibrosis severity

Next, we analyzed transcriptomic datasets from patients with various etiologies of chronic liver disease. In a cohort of 67 patients with MASLD, *ASPN* mRNA levels were positively correlated with fibrosis stage ($r = 0.40$; Fig. 2A). Similarly, in 94 patients with NAFLD, *ASPN* correlated with fibrosis severity ($r = 0.34$; Fig. 2B). Analysis of liver biopsy transcriptomes from 124 patients with chronic hepatitis B revealed that *ASPN* mRNA expression was significantly correlated with both fibrosis stage ($r = 0.33$) and inflammation grade ($r = 0.51$; Fig. 2C and D).

Immunohistochemical staining of liver tissues showed increased Asporin expression with advancing fibrosis stages (Fig. 2E). ImageJ based quantification confirmed a positive correlation between Asporin protein levels and both fibrosis stage ($r = 0.28$; Fig. 2F) and inflammation grade ($r = 0.69$; Fig. 2G).

The prediction of signal peptides using SignalP 6.0[22] identified Asporin as a Sec/SPI-type secreted protein (Supporting Information Fig. S3), implying its viability as a blood-based biomarker. We collected serum samples from 99 patients with liver fibrosis or cirrhosis due to various causes. Asporin levels were positively correlated with FIB-4 scores ($r = 0.39$; Fig. 2H), with an area under the ROC curve (AUC) of 0.81 (Fig. 2I). Asporin levels were negatively correlated with FIB-5 scores ($r = -0.40$; Fig. 2J), with an AUC of 0.76 (Fig. 2K), supporting its potential as a non-invasive fibrosis biomarker.

In a CCl_4 induced liver fibrosis model in C57BL/6 mice, mRNA levels of *Aspn* were markedly elevated in fibrotic liver (Supporting Information Fig. S4A). Analysis of public dataset GSE152329 also confirmed upregulation of *Aspn* in the CCl_4 treated mouse liver (Fig. S4B). Moreover, in the MASLD model reported by Jeong et al.[23], *Aspn* expression progressively increased over time along with fibrosis progression (Fig. S4C), further supporting its association with disease severity.

3.3. ASPN promotes hepatic stellate cell activation and ECM remodeling

We first observed that TGF-β1 stimulation significantly increased *ASPN* expression in LX2 cells (Supporting Information Fig. S5A). Using siRNA to silence *ASPN* during TGF-β1 treatment reduced *COL1A1* mRNA levels (Fig. S5B). An adenoviral vector was used to establish *ASPN* overexpression in LX2 cells for further functional analysis (Fig. S5C).

To investigate the role of *ASPN* in HSC activation, we analyzed single-cell RNA sequencing data from cirrhotic patients (GSE136103). HSC were divided into $ASPN^+$ and $ASPN^-$ subpopulations. Differential expression analysis revealed that fibrosis related genes including *FN1*, *COL1A1*, *COL3A1*, *DCN*, *CTGF*, *TIMP1*, *FBN1*, *POSTN*, *DES*, and *LOX* were significantly upregulated in $ASPN^+$HSC (Fig. 3A and B). GO and Reactome pathway enrichment analyses of the significantly upregulated genes indicated strong enrichment in ECM organization pathways (Supporting Information Fig. S6A and S6B). Consistent results were observed in another single-cell dataset from patients with chronic hepatitis B (GSE186343), where $ASPN^+$HSC also exhibited elevated expression of fibrosis markers (Supporting Information Fig. S7A and S7B), and ECM-related pathways were significantly enriched (Fig. S7C and S7D).

To examine the functional role of *ASPN in vitro*, we performed RNA-seq on LX2 cells with *ASPN* overexpression. Transcriptome analysis revealed 1566 upregulated and 1664 downregulated genes (Fig. 3C). Notably, fibrosis and proliferation related genes such as *COL1A1*, *COL6A2*, *FSCN1* were significantly upregulated (Fig. 3C). We further validated that *ASPN* overexpression in LX2 cells led to increased expression of inflammatory cytokines *IL6* and *TNF*, as well as fibrotic factors *COL1A1*, *TIMP1*, and *ACTA2* (Fig. 3D). Western blot analysis confirmed elevated protein levels of FN1 and Collagen I following Adv-*ASPN* treatment (Fig. 3E). Collagen gel contraction assays revealed enhanced ECM contractility in *ASPN*-overexpressing cells (Fig. 3F). Immunofluorescence staining indicated increased expression of myofibroblast markers α-SMA and Desmin (Fig. 3G and H). In addition, LX2 cells overexpressing *ASPN* exhibited enhanced proliferation and migration, as confirmed by EdU and wound healing assays (Fig. 3I and J). Furthermore, similar profibrotic effects were observed in HSC-T6 cells, where *ASPN* overexpression likewise enhanced FN1 protein levels, promoted cellular proliferation and migration, and increased α-SMA staining (Supporting Information Fig. S8).

3.4. Genetic deletion of ASPN mitigates liver fibrosis in mouse models

To explore the role of *ASPN* in liver fibrosis, we generated whole body *Aspn* knockout (*Aspn*-KO) mice and induced fibrosis using CCl_4. Compared to wild-type (WT) controls, *Aspn*-KO mice exhibited smoother liver surfaces, reduced nodularity, normalized liver-to-body weight ratios, and lower serum AST, ALT, and TC levels (Supporting Information Fig. S9A−S9F). qRT-PCR showed decreased *Col3a1* and *Acta2* expression, and histological staining revealed reduced inflammation, fibrosis, and collagen deposition, with lower Collagen I and α-SMA levels (Fig. S9G−S9I).

Given that *ASPN* is predominantly expressed in HSC, we proceeded to create a conditional knockout ($Aspn^{HSC-KO}$) mouse (Supporting Information Fig. S10). After 6 weeks of CCl_4 administration, gross morphology showed smoother liver surfaces and fewer nodules in CCl_4 treated $Aspn^{HSC-KO}$ mice compared to CCl_4 treated $Aspn^{fl/fl}$ mice (Fig. 4A and B). Ultrasound imaging revealed that $Aspn^{fl/fl}$ mice developed increased hepatic echogenicity, indicative of parenchymal remodeling and collagen accumulation, which was significantly reduced in $Aspn^{HSC-KO}$ mice

followed by Western blot confirming direct interaction between Asporin and ERH. (H) Endogenous co-immunoprecipitation in LX2 cells demonstrating the interaction between Asporin and ERH. (I) SPR sensorgrams showing dose-dependent binding between recombinant Asporin and ERH. (J) LX2 were treated with MG132 to inhibit proteasomal degradation or with cycloheximide (CHX) for indicated time points to block protein synthesis. ERH protein levels were assessed by Western blot. (K) PhosphoSitePlus® database search results showing ERH lysine ubiquitination at residue K12, K41, K84, K90 in human samples. (L) The length of each vertical line is proportional to the confidence score, and brown spheres indicate the predicted residue positions. K12, K37, K75, K77, and K98 were predicted to be high-confidence ubiquitination sites based on sequence features. (M) Structural model of the Asporin−ERH complex generated using AlphaFold2-Multimer, showing a stable interaction involving two binding domains. Hydrogen bond analysis identified Arg13 and Leu95 of ERH forming bonds with Phe77 and Lys27 of Asporin. (N) Hydrophobic interactions between Asporin (Leu26, Met30) and ERH residues (Ile54, Leu57, Leu91−Leu95). M, mol/L.

(Fig. 4C). Doppler imaging further showed that portal vein dilation and decreased flow velocity in $Aspn^{fl/fl}$ were alleviated in $Aspn^{HSC-KO}$ mice, suggesting reduced portal hypertension (Fig. 4C and D). Both liver-to-body weight ratio and hepatic hydroxyproline content were significantly lower in the $Aspn^{HSC-KO}$ group compared to $Aspn^{fl/fl}$ (Fig. 4E and F). Serum ALT, AST, and TC levels were also decreased in $Aspn^{HSC-KO}$ mice (Fig. 4G). qRT-PCR showed reduced expression of Fn1, *Col1a1* and *Acta2* in $Aspn^{HSC-KO}$ livers (Fig. 4H), and Western blot confirmed reduced protein levels of FN1, Collagen I, and α-SMA (Fig. 4I). Histological analyses revealed less inflammation, improved lobular architecture, and reduced collagen deposition and fibrous septa (Fig. 4J). Immunohistochemistry and immunofluorescence further confirmed diminished Collagen I and α-SMA expression (Fig. 4K

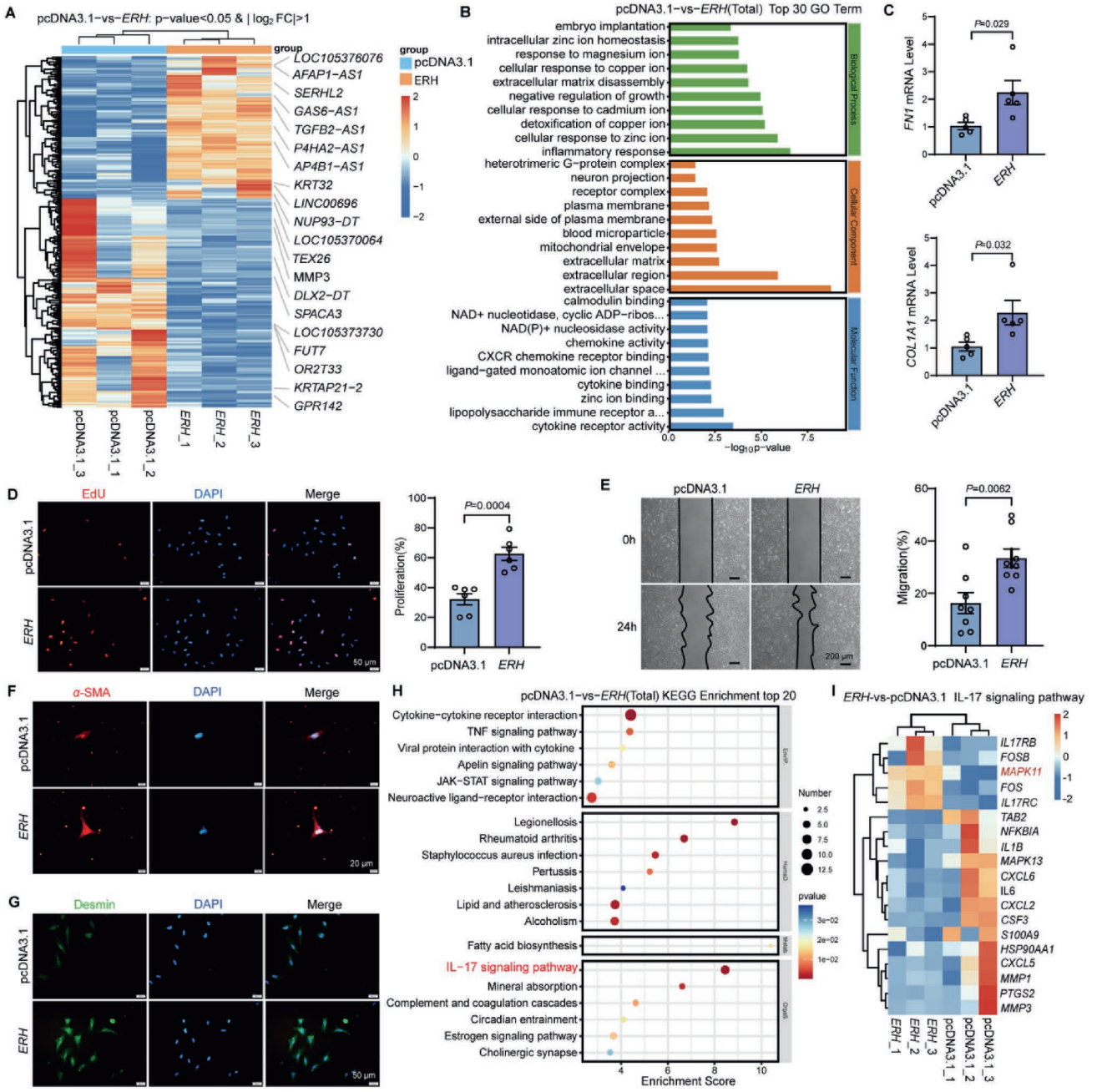

Figure 6 ERH promotes hepatic stellate cell activation *via* IL-17/MAPK11 signaling. (A) RNA-seq analysis of LX2 cells overexpressing *ERH* revealed upregulation of genes related to cell proliferation and migration ($n = 3$, P value < 0.05 & $|\log_2 FC| > 1$). (B) Gene ontology enrichment analysis of differentially expressed genes showed significant enrichment in extracellular space−related pathways (top 30). (C) qRT-PCR validation showing increased expression of fibrogenic marker genes *FN1* and *COL1A1* upon *ERH* overexpression ($n = 4$). (D) EdU proliferation assay ($n = 3$, two images were taken for each group, bar = 200 μm) and (E) wound healing assay ($n = 4$, two images were taken for each group, bar = 50 μm) demonstrating that *ERH* enhances LX2 cell proliferation and migration. (F, G) Immunofluorescence staining showing increased expression of α-SMA ($n = 3$, bar = 20 μm) and Desmin ($n = 3$, bar = 50 μm) in *ERH*-overexpressing LX2 cells. (H) KEGG pathway enrichment analysis revealed that IL-17 signaling is significantly activated by *ERH* overexpression. (I) Heatmap showing that *MAPK11* is upregulated in both *ERH*- and *ASPN*-overexpressing LX2 cells ($n = 3$).

and L). These findings suggest that *Aspn* deletion, particularly in hepatic stellate cells, significantly reduces liver fibrosis. In addition, in the bile duct ligation (BDL)-induced cholestatic fibrosis model, $Aspn^{HSC-KO}$ mice exhibited significantly reduced hepatic hydroxyproline content, lower expression of fibrotic genes, and markedly attenuated collagen deposition and scarring, further supporting the antifibrotic effect of *Aspn* deletion (Supporting Information Fig. S11).

3.5. *Asporin modulates ERH protein stability and downstream fibrogenic signaling*

Since Asporin is a secreted protein, we investigated its paracrine effects on hepatocytes. The co-culture involving LX2 cells overexpressing *ASPN* resulted in a significant upregulation of *Slc27a1* and *Scd1*, genes that play a critical role in lipid metabolism (Supporting Information Fig. S12A and S12B). Moreover, *ASPN* has been implicated in regulating cytoskeletal organization[24]. In control cells, F-actin was thin, peripheral, and lacked stress fibers. In contrast, *ASPN*-overexpressing cells displayed thick stress fibers and a spindle-shaped morphology, indicating activation and contractility typical of migrating and proliferating HSC (Fig. S12C).

To further elucidate the intracellular mechanisms of Asporin function, we performed GST pull-down followed by mass spectrometry to identify Asporin interacting proteins (Fig. 5A–C). A total of 185 candidate binding proteins were identified (Fig. 5D). KEGG enrichment analysis indicated a predominant association with cytoskeletal proteins (Fig. 5E).

Subcellular fractionation revealed increased Asporin levels upon TGF-β1 stimulation, with predominant enrichment in the nuclear fraction (Supporting Information Fig. S13A). Among the candidate interactors identified by mass spectrometry, ERH was detected (Fig. 5F, Supporting Information Table S4) and shown to be upregulated in the nucleus of TGF-β1 treated LX2 cells (Fig. S13B). GST pull-down followed by Western blot validated the direct interaction between Asporin and ERH (Fig. 5G). This interaction was further validated by endogenous co-immunoprecipitation (Fig. 5H) and SPR analysis, which demonstrated concentration dependent binding kinetics between recombinant Asporin and ERH (Fig. 5I). Asporin overexpression led to increased ERH protein levels (Fig. S13C). Furthermore, treatment of LX2 cells with MG132 (a proteasome inhibitor) and cycloheximide (CHX, a protein synthesis inhibitor) revealed that Asporin inhibited the ubiquitin-mediated degradation of ERH, suggesting that Asporin stabilizes ERH protein levels by attenuating its proteasomal turnover (Fig. 5J).

To determine whether Asporin regulates ERH *via* post-translational modification, we first queried the PhosphoSitePlus® database, which identified several lysine residues (K12, K41, K84, K90) as ubiquitination sites on human ERH (Fig. 5K). We then conducted an *in silico* analysis to predict additional ubiquitination-prone lysine residues. Among the ten lysine residues in ERH, five (K12, K37, K75, K77, and K98) were predicted as high confidence ubiquitination site (Fig. 5L). These findings identify K12 as a

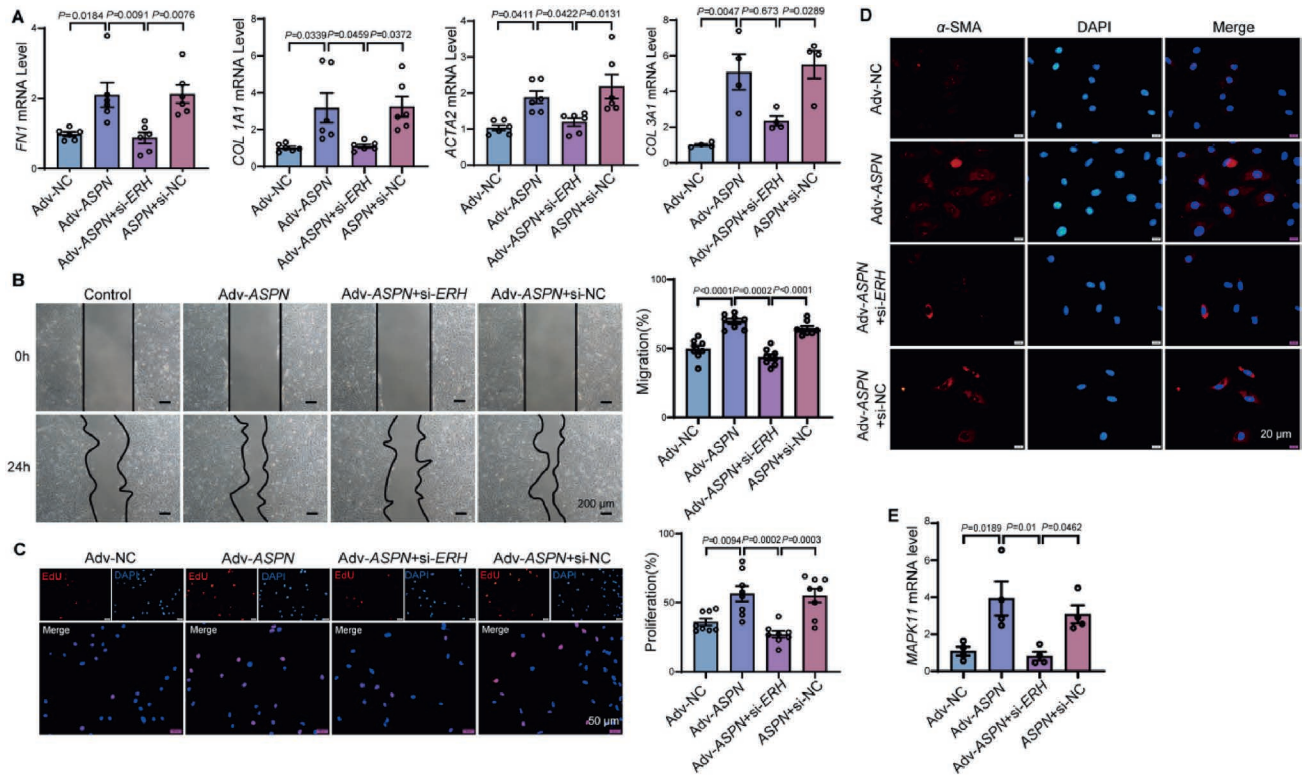

Figure 7 ERH is a key mediator of Asporin-induced hepatic stellate cell activation. (A) qRT-PCR analysis showing that *ERH* knockdown partially reverses *ASPN*-induced upregulation of fibrogenic genes *FN1* ($n = 6$), *COL1A1* ($n = 6$), *ACTA2* ($n = 6$), *COL3A1* ($n = 4$) in LX2 cells. (B) Wound healing assay ($n = 4$, two images were taken for each group, bar = 200 μm) and (C) EdU proliferation assay ($n = 4$, two images were taken for each group, bar = 50 μm) showing that *ERH* knockdown suppresses *ASPN*-mediated migration and proliferation of LX2 cells. (D) Immunofluorescence staining showing reduced α-SMA protein expression in *ASPN* overexpressing LX2 cells after *ERH* silencing ($n = 4$, bar = 20 μm). (E) qRT-PCR analysis showing that *ERH* knockdown significantly reduces *MAPK11* expression induced by *ASPN* ($n = 4$).

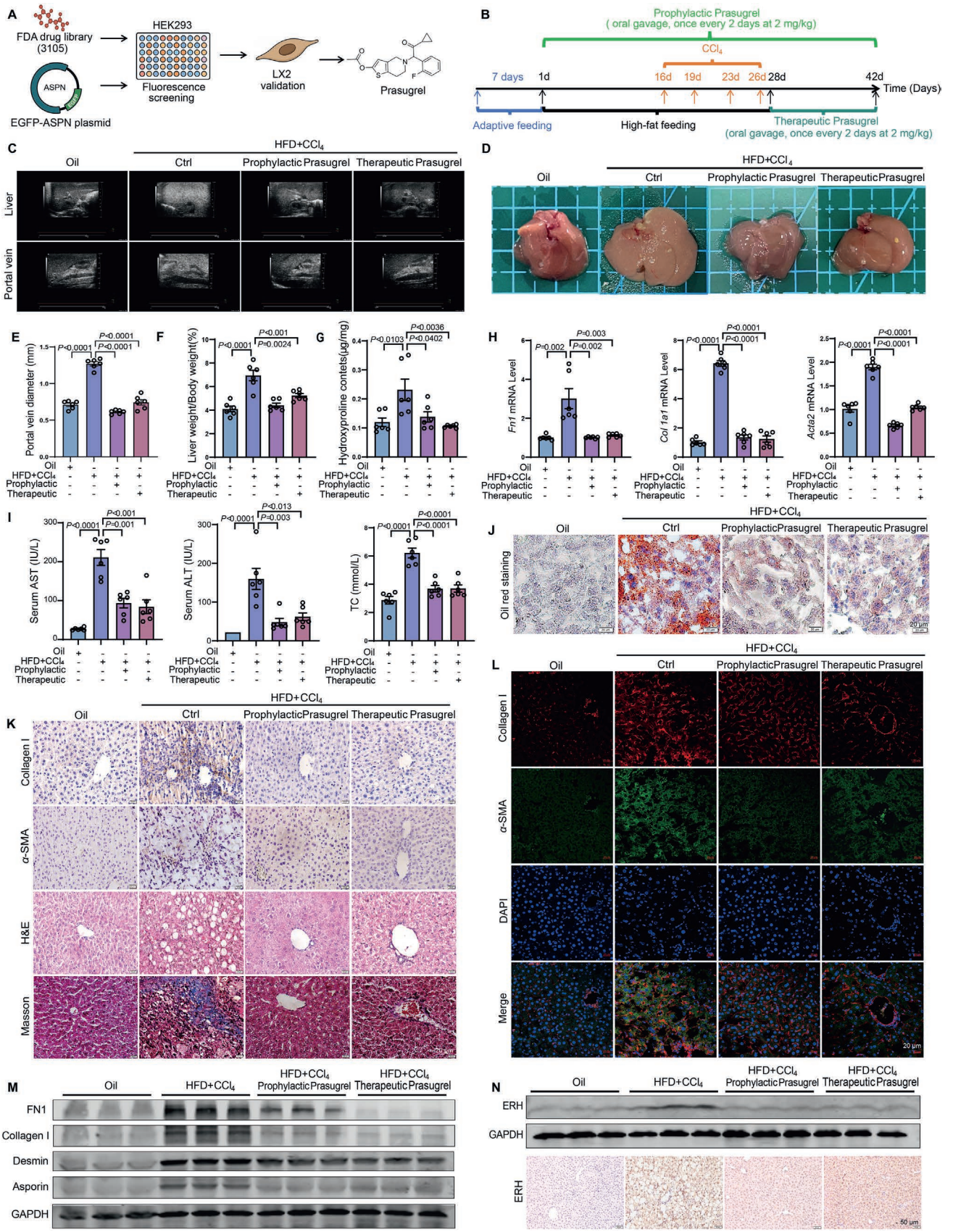

Figure 8 Prasugrel inhibits Asporin expression and attenuates liver fibrosis *in vivo*. (A) High-throughput screening of 3105 FDA-approved compounds in EGFP-*ASPN*-transfected cells identified prasugrel as a potential Asporin inhibitor. (B) Schematic diagram of the experimental workflow for prasugrel intervention in a mouse model of liver fibrosis induced by high-fat diet and CCl_4 administration. (C) Representative

conserved and likely functionally critical site for ERH ubiquitination, and suggest a mechanism by which Asporin may modulate ERH stability by interfering with ubiquitination at this residue. Using the AlphaFold2-Multimer model, we predicted the Asporin−ERH complex structure and found that Asporin interacts with ERH *via* two distinct domains, forming a stable conformation. Key residues mediating hydrogen bonding include ERH Arg13 and Leu95 with Asporin Phe77 and Lys27, while hydrophobic contacts involve Asporin Leu26 and Met30 with multiple ERH residues (Fig. 5M and N). Notably, the proximity of ERH K13 to the predicted ubiquitination site K12 implies that Asporin may sterically hinder ubiquitin ligase access, thereby reducing ERH ubiquitination.

3.6. ERH mediates the pro-fibrotic effects of Asporin via the IL-17/MAPK11 signaling

To explore the role of ERH in liver fibrosis, we overexpressed ERH in LX2 cells and conducted RNA-seq, which revealed upregulation of genes related to cell proliferation, migration, and extracellular space (Fig. 6A and B). qRT-PCR validation confirmed that ERH upregulated the expression of fibrosis related genes *FN1* and *COL1A1* (Fig. 6C). EdU and wound healing assays showed that ERH promoted LX2 proliferation and migration (Fig. 6D and E). Immunofluorescence staining further showed that ERH overexpression enhanced the expression of activation markers α-SMA and Desmin at the protein level (Fig. 6F and G), indicating a pro-activation effect on HSC. Pathway enrichment analysis identified the IL-17 signaling pathway as the most significantly upregulated upon ERH overexpression (Fig. 6H), with *MAPK11* expression notably increased in both ERH and *ASPN* overexpressing cells (Fig. 6I, Supporting Information Fig. S14), suggesting *MAPK11* may serve as a common downstream effector of Asporin and ERH.

To further confirm the role of ERH in Asporin mediated signaling, we performed rescue experiments by co-transfecting *ERH* siRNA in *ASPN*-overexpressing LX2 cells. Knockdown of *ERH* partially reversed the *ASPN*-induced upregulation of fibrogenic genes *FN1*, *COL1A1*, *ACTA2*, and *COL3A1* (Fig. 7A). *ERH* silencing also attenuated *ASPN*-driven proliferation and migration, as demonstrated by EdU and wound-healing assays (Fig. 7B and C), and reduced α-SMA protein expression as shown by immunofluorescence staining (Fig. 7D). Importantly, si-*ERH* alone did not markedly affect proliferation or migration in Adv-NC treated cells, whereas it abolished the pro-proliferative and pro-migratory effects induced by *ASPN* overexpression (Supporting Information Fig. S15). Moreover, ASPN induced *MAPK11* upregulation was markedly suppressed upon ERH knockdown (Fig. 7E). Collectively, these findings demonstrate that ERH acts as a critical mediator of *ASPN* driven fibrogenic signaling, potentially through regulation of the IL-17/MAPK11 pathway.

3.7. Prasugrel suppresses Asporin and alleviates liver fibrosis in vivo

To identify Asporin targeting compounds, we performed an absorbance based EGFP-*ASPN* reporter screen in HEK293 cells and a secondary functional validation in LX2 cells, identifying prasugrel as the most robust suppressor of Asporin activity (Fig. 8A, Supporting Information Fig. S16A and S16B). Subsequent molecular docking and SPR measurements confirmed direct binding between prasugrel and Asporin, substantiating its target specificity (Fig. S16C and S16D).

We established a comprehensive mouse model of liver fibrosis using a combination of high-fat diet feeding and CCl_4 injection. Mice were treated with prasugrel either preventively or therapeutically (Fig. 8B). Ultrasound examination revealed improved liver echotexture and reduced fibrotic features in prasugrel-treated mice compared to untreated fibrotic controls (Fig. 8C). Upon sacrifice, macroscopic inspection showed that livers from control mice had a smooth and reddish surface, whereas those from the fibrosis model group exhibited coarse surfaces with visible nodular lesions. In contrast, the livers from prasugrel treated mice showed marked improvement in surface smoothness and reduced nodularity (Fig. 8D).

Measurement of portal vein diameter showed a significant reduction in prasugrel treated mice (Fig. 8E). The liver-to-body weight ratio, which was significantly increased in fibrotic mice, was restored to near-normal levels following prasugrel treatment (Fig. 8F). Consistently, hydroxyproline content analysis confirmed reduced collagen deposition after prasugrel administration, accompanied by decreased mRNA expression of *Fn1*, *Col1a1*, and *Acta2* (Fig. 8G and H). Serum ALT, AST, and TC levels were significantly decreased after prasugrel treatment (Fig. 8I). Oil Red O staining showed lipid droplet accumulation in fibrotic livers, which was alleviated by prasugrel (Fig. 8J). Prasugrel also suppressed Collagen I and α-SMA expression, as shown by immunohistochemistry and immunofluorescence (Fig. 8K and L). H&E and Masson staining revealed that prasugrel improved inflammation, lobular disruption, and collagen deposition observed in the model group (Fig. 8K).

Western blot analysis showed that prasugrel treatment reduced the protein levels of FN1, Collagen I, and Desmin, along with the key regulatory proteins Asporin (Fig. 8M). Consistently, ERH expression was reduced in liver tissues following prasugrel treatment (Fig. 8N).

4. Discussion

In this study, we systematically identified Asporin as a novel profibrotic driver and potential therapeutic target in liver fibrosis. Through integrated analysis of human single-cell transcriptomes,

ultrasound images showing improved liver echotexture in prasugrel-treated mice ($n = 6$). (D) Gross liver morphology in each group ($n = 6$). (E) Portal vein diameter was significantly reduced in prasugrel-treated mice ($n = 6$). (F, G) Liver-to-body weight ratio and hepatic hydroxyproline content were decreased in the prasugrel group, indicating reduced collagen deposition ($n = 6$). (H) qRT-PCR analysis showing that prasugrel suppressed the mRNA expression of *Fn1*, *Col1a1*, and *Acta2* ($n = 6$). (I) Serum ALT, AST, and total cholesterol levels were significantly reduced in prasugrel-treated mice ($n = 6$). (J) Oil Red O staining showing reduced hepatic lipid accumulation in the prasugrel group ($n = 3$, bar = 20 μm). (K) Representative images of liver histology. Upper panels: Immunohistochemical staining of α-SMA and Collagen I in liver tissues. Lower panels: H&E staining and Masson's trichrome staining ($n = 3$, bar = 20 μm). (L) Immunofluorescence staining of α-SMA and Collagen I in liver tissues ($n = 3$, bar = 20 μm). (M) Western blot analysis showing decreased protein levels of FN1, collagen I, Desmin and Asporin in liver tissues following prasugrel treatment ($n = 3$). (N) Western blot and immunohistochemical staining confirm reduced ERH expression in prasugrel-treated liver tissues ($n = 3$, bar = 50 μm).

bulk tissue datasets, clinical cohorts, and murine models, we provide compelling evidence that Asporin is selectively upregulated in pathogenic hepatic stellate cells, and promotes liver fibrosis *via* stabilization of the nuclear protein ERH and activation of IL-17 signaling. These findings uncover a previously unrecognized post-translational mechanism of fibrogenesis and highlight the Asporin−ERH axis as a promising therapeutic target.

Our single-cell analysis revealed that *ASPN* expression is specifically enriched in HSC subpopulations with high fibrogenic and inflammatory activity. These subtypes were markedly expanded in fibrotic liver tissues, and pseudotime analysis further demonstrated that *ASPN* expression increases progressively along the trajectory of HSC activation. This spatial-temporal enrichment supports a model in which Asporin actively contributes to HSC activation rather than serving as a passive fibrosis marker. Importantly, this association was not limited to transcriptomic datasets. We demonstrated that Asporin expression in both liver tissue and serum positively correlates with fibrosis stage and inflammatory grade in diverse clinical cohorts, including MASLD, NAFLD, and chronic hepatitis B. Moreover, serum Asporin levels showed strong diagnostic potential with AUC values exceeding 0.80 in ROC analyses, supporting its potential as a non-invasive biomarker for fibrosis surveillance, potentially outperforming indices such as FIB-4 and FIB-5.

Mechanistically, we identified ERH as a novel intracellular binding partner of Asporin using GST pull-down and mass spectrometry. While ERH has been characterized as a nuclear regulator of RNA splicing, mitosis, and genome maintenance[25,26], its role in liver fibrosis had not been previously described. We demonstrated that Asporin binds directly to ERH and inhibits its ubiquitin-mediated degradation, thereby stabilizing ERH protein levels. Structural modeling revealed that Asporin masks the K12 ubiquitination site on ERH through hydrogen bonds and hydrophobic interactions, providing a plausible mechanism for this stabilization. Notably, ERH overexpression recapitulated the fibrogenic effects of Asporin, promoting HSC proliferation, migration, and ECM remodeling. Rescue experiments further confirmed that knockdown of ERH abrogates the fibrogenic effects of Asporin, underscoring ERH as a functional mediator of Asporin induced fibrosis.

One novel insight from our study is the implication of the IL-17/MAPK11 signaling axis downstream of the Asporin−ERH pathway. IL-17 cytokines have been shown to contribute to liver fibrosis by driving inflammation and promoting HSC activation[27,28]. MAPK11 (also known as p38β) is not only a key kinase in the MAPK signaling cascade but also functions as a downstream effector of IL-17 signaling, mediating cellular responses such as proliferation[29], inflammatory disorders[30] and fibrosis[31]. Our findings reveal that both Asporin and ERH upregulate *MAPK11* expression, suggesting a coordinated mechanism through which stromal Asporin and nuclear ERH converge to activate the *MAPK11*-dependent profibrotic program.

The translational relevance of our findings was supported by extensive *in vivo* validation. Both global and HSC specific knockout of *Aspn* in mice significantly attenuated CCl_4-induced liver fibrosis, improving liver architecture, reducing collagen accumulation, and normalizing serum liver injury markers. These findings provide direct genetic evidence for a cell autonomous profibrotic role of Asporin in HSC. Moreover, we identified prasugrel, an FDA approved P2Y12 inhibitor, as a potent Asporin suppressor *via* high-throughput drug screening. Prasugrel administration in a CCl_4 + HFD fibrosis model effectively reduced Asporin and ERH protein levels, improved histopathological features, and alleviated portal hypertension and lipid accumulation. These data indicate that pharmacological inhibition of Asporin may offer a viable antifibrotic strategy with potential for clinical translation.

Despite these strengths, our study has several limitations. While Asporin's role was validated in multiple models and patient cohorts, its diagnostic and therapeutic value requires further validation in larger prospective cohorts and in other liver injury types such as cholestatic disease. Although ERH was identified as a key effector, additional intracellular or extracellular Asporin partners may exist and warrant systematic interactome mapping. Finally, the long-term safety and liver specificity of prasugrel as an Asporin targeting agent require further preclinical and clinical evaluation.

5. Conclusions

In conclusion, our study identifies Asporin as a critical regulator of HSC activation and liver fibrosis progression. We establish Asporin as both a diagnostic biomarker and a therapeutic target, and reveal a novel intracellular mechanism involving the stabilization of ERH. Our work opens new avenues for understanding fibrosis biology and offers a promising targetable pathway for antifibrotic therapy in chronic liver disease.

Acknowledgments

We thank Prof. Yang Zhang very much for providing AML-12 cells. The experimental item images and graphical abstract were drawn by Figdraw (www.figdraw.com) (authorization code: WATPR90b60, PYOUSb61b7 and USPWA73373). ChatGPT-4o (OpenAI, USA) was used exclusively for language polishing and error checking.

This study was supported by the National Natural Science Foundation of China (U24A20645, 82200070, and 82304589); the National Multidisciplinary Innovation Team Project in Traditional Chinese Medicine (ZYYCXTD-D-202407); Fellowship of China Postdoctoral Science Foundation (2024M763877, 2025T180632); Chongqing Special Postdoctoral Science Foundation (2024CQBSHTB3042, China); Key Project of the Scientific and Technological Research Program of Chongqing Municipal Education Commission (KJZD-K202500104, China); The Science and Technology Planning Project of Guangzhou (2024A03J0377, China).

Author contributions

Conception and design of the study: Haihai Liang, Tianyu Li, Jing Liu, Yanyan Liu; Acquisition of data: Jian Sun, Ruoxuan Yang, Mengmeng Liu, Yi Chen, Yu Zhang, Huiying Gao, Zhiwei Ning, Shifen Li, Dina Saifullina, Xiaomu Tian, Tongzhu Jin, Yingying Guo, Qianqian Wang, Yixin Zhang, Tengfei Pan, Yu Bian, Erliang Guo, Jing Liu; Analysis and interpretation of data: Jian Sun, Ruoxuan Yang, Mengmeng Liu, Yi Chen, Yu Zhang, Haihai Liang, Tianyu Li; Drafting of the article: Jian Sun, Ruoxuan Yang, Mengmeng Liu, Yi Chen; Critical revision of the article for important intellectual content: Haihai Liang, Tianyu Li, Jing Liu, Yanyan Liu; Final approval of the version to be published: All authors.

Conflicts of interest

The authors declared no conflicts of interest.

Appendix A. Supporting information

Supporting information to this article can be found online at https://doi.org/10.1016/j.apsb.2026.03.045.

References

1. Huang DQ, Terrault NA, Tacke F, Gluud LL, Arrese M, Bugianesi E, et al. Global epidemiology of cirrhosis—Aetiology, trends and predictions. *Nat Rev Gastroenterol Hepatol* 2023;**20**:388−98.
2. Kisseleva T, Brenner D. Molecular and cellular mechanisms of liver fibrosis and its regression. *Nat Rev Gastroenterol Hepatol* 2021;**18**: 151−66.
3. Kim HY, Yu JH, Chon YE, Kim SU, Kim MN, Han JW, et al. Prevalence of clinically significant liver fibrosis in the general population: a systematic review and meta-analysis. *Clin Mol Hepatol* 2024;**30**: S199−213.
4. Younossi ZM, Paik JM, Lazarus JV, Burra P, Eguchi Y, Tacke F, et al. Projected global clinical, humanistic, and economic impact of metabolic dysfunction-associated steatohepatitis (MASH): the cost of inaction based on data from nine countries. *Clin Gastroenterol Hepatol* 2026;**24**:1016−34.
5. Ginès P, Castera L, Lammert F, Graupera I, Serra-Burriel M, Allen AM, et al. Population screening for liver fibrosis: toward early diagnosis and intervention for chronic liver diseases. *Hepatology* 2022;**75**:219−28.
6. Hunold T, Govalan R, Parikh N. Biomarkers for the diagnosis of cirrhosis and cirrhosis-related complications. *Gastroenterol Clin N Am* 2026;**55**:203−16.
7. Hinkson A, Lally H, Gibson H, Jones R, Rowe IA, Shinkins B, et al. Meta-analysis: enhanced liver fibrosis test to identify hepatic fibrosis in chronic liver diseases. *Aliment Pharmacol Ther* 2023;**57**:750−62.
8. Jing H, Ren Y, Zhou Y, Xu M, Krizkova S, Heger Z, et al. Remodeling of the liver fibrosis microenvironment based on nilotinib-loaded multicatalytic nanozymes with boosted antifibrogenic activity. *Acta Pharm Sin B* 2023;**13**:5030−47.
9. Gilgenkrantz H, Sayegh RA, Lotersztajn S. Immunoregulation of liver fibrosis: new opportunities for antifibrotic therapy. *Annu Rev Pharmacol Toxicol* 2025;**65**:281−99.
10. Liu R, Li Y, Zheng Q, Ding M, Zhou H, Li X. Epigenetic modification in liver fibrosis: promising therapeutic direction with significant challenges ahead. *Acta Pharm Sin B* 2024;**14**:1009−29.
11. Geng Y, Schwabe RF. Hepatic stellate cell heterogeneity: functional aspects and therapeutic implications. *Hepatology* 2025. Available form: https://doi.org/10.1097/HEP.0000000000001386.
12. Schwabe RF, Brenner DA. Hepatic stellate cells: balancing homeostasis, hepatoprotection and fibrogenesis in health and disease. *Nat Rev Gastroenterol Hepatol* 2025;**22**:481−99.
13. Akkız H, Gieseler RK, Canbay A. Liver fibrosis: from basic science towards clinical progress, focusing on the central role of hepatic stellate cells. *Int J Mol Sci* 2024;**25**:7873.
14. Watson BR, Paul B, Rahman RU, Amir-Zilberstein L, Segerstolpe Å, Epstein ET, et al. Spatial transcriptomics of healthy and fibrotic human liver at single-cell resolution. *Nat Commun* 2025;**16**:319.
15. Ramachandran P, Dobie R, Wilson-Kanamori JR, Dora EF, Henderson BEP, Luu NT, et al. Resolving the fibrotic niche of human liver cirrhosis at single-cell level. *Nature* 2019;**575**:512−8.
16. Huang Y, Pu W, Wang L, Ma Q, Ma Y, Liu Q, et al. Atypical chemokine receptor 1-positive endothelial cells mediate leucocyte infiltration and synergize with secreted frizzled-related protein 2/asporin-positive fibroblasts to promote skin fibrosis in systemic sclerosis. *Br J Dermatol* 2024;**191**:964−78.
17. Iqbal S, Andersson S, Nesta E, Pentinmikko N, Kumar A, Kumar Jha S, et al. Fetal-like reversion in the regenerating intestine is regulated by mesenchymal asporin. *Cell Stem Cell* 2025;**32**. 613-26.e8.
18. Medzikovic L, Aryan L, Ruffenach G, Li M, Savalli N, Sun W, et al. Myocardial fibrosis and calcification are attenuated by microRNA-129-5p targeting Asporin and Sox9 in cardiac fibroblasts. *JCI Insight* 2023;**8**:e168655.
19. Ge S, Cen J, Liu X, Hong Y, Tang Y, Yu Y, et al. TGFβ-activated Asporin interacts with STMN1 to promote prostate cancer docetaxel chemoresistance and metastasis by upregulating the Wnt/β-catenin signaling pathway. *Drug Resist Updates* 2025;**81**:101227.
20. Kumagai H, Sasaki A, Umemura A, Kakisaka K, Iwaya T, Sn S. Effects of laparoscopic sleeve gastrectomy on nonalcoholic fatty liver disease and TGF-β signaling pathway. *Endocr J* 2024;**71**: 139−52.
21. Radivojac P, Vacic V, Haynes C, Cocklin RR, Mohan A, Heyen JW, et al. Identification, analysis, and prediction of protein ubiquitination sites. *Proteins* 2010;**78**:365−80.
22. Teufel F, Almagro Armenteros JJ, Johansen AR, Gíslason MH, Pihl SI, Tsirigos KD, et al. SignalP 6.0 predicts all five types of signal peptides using protein language models. *Nat Biotechnol* 2022;**40**: 1023−5.
23. Jeong BK, Choi WI, Choi W, Moon J, Lee WH, Choi C, et al. A male mouse model for metabolic dysfunction-associated steatotic liver disease and hepatocellular carcinoma. *Nat Commun* 2024;**15**: 6506.
24. Liu L, Yu H, Long Y, You Z, Ogawa R, Du Y, et al. Asporin inhibits collagen matrix-mediated intercellular mechanocommunications between fibroblasts during keloid progression. *FASEB J* 2021;**35**:e21705.
25. Weng MT, Luo J. The enigmatic ERH protein: its role in cell cycle, RNA splicing and cancer. *Protein Cell* 2013;**4**:807−12.
26. Kozlowski P. Thirty years with ERH: an mRNA splicing and mitosis factor only or rather a novel genome integrity protector?. *Cells* 2023; **12**:2449.
27. Fabre T, Kared H, Friedman SL, Shoukry NH. IL-17A enhances the expression of profibrotic genes through upregulation of the TGF-β receptor on hepatic stellate cells in a JNK-dependent manner. *J Immunol* 2014;**193**:3925−33.
28. Hu T, Chen M, Tian S, Luo P, Zhang J. Mechanistic studies on the role of IL-17/NLRP3 in arsenic-induced activation of hepatic stellate cells through hepatocyte proptosis. *Toxics* 2025;**13**:287.
29. Liu Y, Wang G, Jiang X, Li W, Zhai C, Shang F, et al. TRIM67 inhibits tumor proliferation and metastasis by mediating MAPK11 in colorectal cancer. *J Cancer* 2020;**11**:6025−37.
30. Pelaia C, Vatrella A, Sciacqua A, Terracciano R, Pelaia G. Role of p38-mitogen-activated protein kinase in COPD: pathobiological implications and therapeutic perspectives. *Expet Rev Respir Med* 2020; **14**:485−91.
31. Zhang S, Weinheimer C, Courtois M, Kovacs A, Zhang CE, Cheng AM, et al. The role of the Grb2−p38 MAPK signaling pathway in cardiac hypertrophy and fibrosis. *J Clin Investig* 2003;**111**: 833−41.